

# Skin biomedical optical imaging system using dual-wavelength polarimetric control with liquid crystals

**Avner Safrani**

**Ofir Aharon**

**Shahar Mor**

Ben Gurion University of the Negev  
Department of Electro-Optic Engineering  
Beer Sheva, 84105 Israel

**Ofer Arnon**

**Lior Rosenberg**

Ben Gurion University of the Negev  
Soroka University Medical Center  
Department of Plastic and Reconstructive Surgery  
and Burn Unit  
Beer Sheva, 84105 Israel

**Ibrahim Abdulhalim**

Ben Gurion University of the Negev  
Department of Electro-Optic Engineering  
Beer Sheva, 84105 Israel

## 1 Introduction

The skin is the outer coverage of the body and its largest organ. The skin covers and protects the underlying muscles, bones, ligaments, and internal organs. Its main functions are to provide sensation, insulation, and temperature regulation and to protect the body from water loss, pathogen exposure, injuries, chemical insults, and ultraviolet (UV) radiation. The skin may be damaged by external and internal insults such as burns, injuries and tumors. The process in which it repairs the damage is called “wound healing” and ends by the epithelialization of preserved dermis or formation of a scar. During the phase of wound healing, the border between healthy and damaged tissues is difficult or even impossible to define due to the inflammatory and regenerative process. The significance in determining healthy borders arises mainly in treatments of tumors, moles, and other cutaneous lesions. The shape of the borders of a mole is one of the key factors in the clinical diagnosis of skin cancer, where dermatologists use four parameters to indicate malignancy potential (ABCD), in which two of them, A and B—*asymmetry and borders*, define the lesion interface with the normal tissues. In melanoma skin cancer, the most deadly skin cancer type, the importance of noninvasive, fast early detection is extremely significant. Melanoma is irregularly proliferating pigmented melanocyte cells. If not treated in early stages, melanoma can metastasize to vital organs and eventually cause death. At present, the currently used diagnostic technique for melanoma detection is the expert’s visual assessment, sometimes with the assistance of a dermatoscope. At present, definite diagnosis can be achieved only by invasive tissue biopsy or excisional biopsy.

**Abstract.** Spectropolarimetric skin imaging is becoming an attractive technique for early detection of skin cancer. Using two liquid crystal retarders in combination with a dual-band passive spectral filter and two linear polarizers, we demonstrate the spectral and polarimetric imaging of skin tissue in the near infrared. Based on this concept, a compact prototype module has been built and is being used for clinical evaluation. © 2010 Society of Photo-Optical Instrumentation Engineers. [DOI: 10.1117/1.3394338]

**Keywords:** skin imaging; skin cancer; spectral imaging; polarimetric imaging.

Paper 09349R received Aug. 12, 2009; revised manuscript received Dec. 14, 2009; accepted for publication Mar. 3, 2010; published online Apr. 19, 2010.

A noninvasive technique for accurate early detection of skin cancer and its boundaries could be an important tool in this field. Hence, by providing high-resolution images of the borders of skin lesions, both of the superficial and of deep layers of the skin, dermatologists may have faster and better diagnosis. Another important aspect of correctly defining the borders of a lesion is related to cosmetics. Sun-exposed skin is prone to develop nonpigmented lesions from the group of basal cell carcinoma (BCC; as many as 75% of all the skin cancer cases) and squamous cell carcinoma (SCC; as many as 20%). Since the face and the neck are the most exposed areas, they are most prone to develop these lesions.<sup>1</sup> The tendency to limit excision to a minimum because of cosmetic considerations indicates a need for accurate definition of the borders (B) of these tumors both on the superficial layer and underneath the skin.

During the last couple of decades, several noninvasive methods were suggested, among them methods based on light scattering,<sup>2,3</sup> confocal microscopy,<sup>4</sup> photo-acoustic microscopy,<sup>5</sup> optical coherence tomography (OCT),<sup>6–8</sup> polarimetric imaging,<sup>9–11</sup> and spectropolarimetric (SP) imaging.<sup>1,12,13</sup> In the SP imaging method, images are acquired at different wavelengths and different linear polarization states. Usually, two polarized images are used, one with a parallel polarizer and analyzer and the second with crossed polarizers. The subtraction of the perpendicular polarization image from the parallel polarization image provides an image that is mainly composed of the superficial layer of the skin (0.1 to 0.3 mm), whereas the subtraction of the spectrally resolved images provides an image of deeper skin layers (down to 1 mm).<sup>9</sup> The SP method holds several advantages with respect to other methods. With respect to the confocal, OCT,

Address all correspondence to: Ibrahim Abdulhalim, Ben Gurion University of the Negev, Department of Electro-Optic Engineering, Beer Sheva, 84105 Israel. Tel: 972-8-6479803; Fax: 972-8-6479494; E-mail: abdulhl@bgu.ac.il

and photo-acoustic microscopy methods, it is much faster and cheaper; in comparison to scattering methods, it is faster and provides a visualization of the lesion; in comparison to the polarimetric-only method, it has an additional degree of freedom by providing spectrally resolved images and thus deeper skin layer images with improved contrast due to different absorption and scattering characteristics of benign and malignant tissues. In SP, it is important to be able to scan the wavelength and polarization fast enough both for the convenience of the patient and doctor and to prevent the blurring effects of unintentional movements. Compactness and miniaturization are important factors for the ease of use. Recently, we have developed several liquid crystal (LC) tunable filters<sup>14,15</sup> and polarization control<sup>16</sup> devices for the purpose of using them in biomedical optical imaging systems. In this study, we present one implementation of these concepts by which we acquire polarimetric images at two different wavelengths controlled with simple LC retarders in the near infrared (NIR).

## 2 Liquid Crystal NIR Dual-Wavelength Polarization Controller

The following spectropolarimetric method uses an LC device that generates different wavelength polarization modes. We present the theoretical bases, as well as the practical performances of the diagnostic LC device.

### 2.1 Theoretical Design

The device's optical configuration is depicted in Fig. 1. The light entering the device is linearly polarized along the  $x$ -axis direction by the first polarizer (P1), followed by a liquid crystal retarder (LCR1), which is aligned with its optical axis at 45 deg with respect to the  $y$  axis. (Here,  $n_o$  and  $n_e$  are the ordinary and extraordinary refractive indices of the liquid crystal cell.) The light is then transmitted toward the second polarizer (P2), which is parallel to the first polarizer. An additional LC retarder, LCR2, which is parallel to LCR1, is

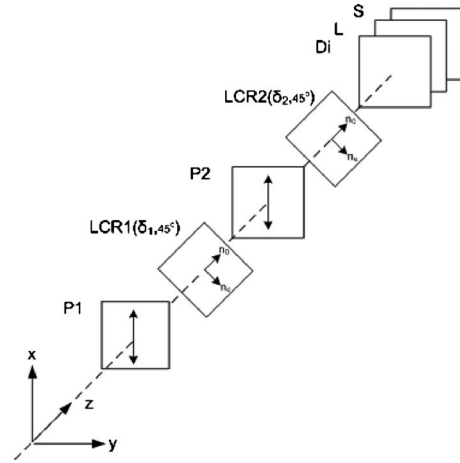


**Fig. 1** The optical stack comprising the LC device for the wavelength and polarization control.

positioned after the second polarizer. Last, a dielectric mirror (Di), an optical long-pass filter (L), and an optical short-pass filter (S) are positioned at the end of the optical stack.

The output field that is transmitted through the optical components in Fig. 1 is given by the Jones matrix multiplications, as follows:

$$\begin{aligned} \vec{E}_{OUT} = & S(\omega_{HPF}) \cdot L(\omega_{LPF}) \cdot Di(\Delta\omega) \cdot LCR2(\delta_2, 45 \text{ deg}) \\ & \cdot P2(0 \text{ deg}) \cdot LCR1(\delta_1, 45 \text{ deg}) \\ & \cdot P1(0 \text{ deg}) \vec{E}_{IN,0} \exp(i\omega t), \end{aligned} \quad (1)$$

where the input electrical field vector is  $\vec{E}_{IN,0}$ , and  $\omega$  is its frequency.  $\omega_{HPF}$  and  $\omega_{LPF}$  are the cutoff frequencies of the short-pass filter and long-pass filter, respectively, and  $\Delta\omega = \omega_2 - \omega_1$  is the forbidden frequency band of the dielectric mirror. The retardation of the LCRs is denoted as  $\delta$  [ $\delta = 2\pi d(n_e - n_o)/\lambda$ ], and it is controlled by voltage. Thus, the Jones matrices formalism<sup>17</sup> of Eq. (1) is:

$$\begin{aligned} \vec{E}_{OUT} = & \begin{bmatrix} u(\omega - \omega_{HPF}) & 0 \\ 0 & u(\omega - \omega_{HPF}) \end{bmatrix} \begin{bmatrix} 1 - u(\omega - \omega_{LPF}) & 0 \\ 0 & 1 - u(\omega - \omega_{LPF}) \end{bmatrix} \\ & \times \begin{bmatrix} 1 - u(\omega - \omega_1) + u(\omega - \omega_2) & 0 \\ 0 & 1 - u(\omega - \omega_1) + u(\omega - \omega_2) \end{bmatrix} \times \exp(i\beta_2) \begin{bmatrix} \cos \delta_2/2 & -i \sin \delta_2/2 \\ -i \sin \delta_2/2 & \cos \delta_2/2 \end{bmatrix} \times \begin{bmatrix} 1 & 0 \\ 0 & 0 \end{bmatrix} \exp(i\beta_1) \\ & \times \begin{bmatrix} \cos \delta_1/2 & -i \sin \delta_1/2 \\ -i \sin \delta_1/2 & \cos \delta_1/2 \end{bmatrix} \begin{bmatrix} 1 & 0 \\ 0 & 0 \end{bmatrix} \vec{E}_{IN,0} \exp(i\omega t), \end{aligned} \quad (2)$$

where  $\beta_{1,2}$  are the average phase accumulations [ $\beta = 2\pi d(n_e + n_o)/\lambda$ ] in passing through the retarders, and the function  $u$  is a unit step function,

$$u(x) = \begin{cases} 1, & x \geq 0 \\ 0 & \text{else} \end{cases}. \quad (3)$$

By performing the multiplication, the resulting electric field is given by Eq. (4):

$$\vec{E}_{OUT} = u(\omega - \omega_{HPF})[1 - u(\omega - \omega_{LPF})][1 - u(\omega - \omega_1) + u(\omega - \omega_2)] \times \begin{bmatrix} \cos \delta_2/2 \cos \delta_1/2 \\ -i \sin \delta_2/2 \cos \delta_1/2 \end{bmatrix} E_{IN,0,X} \exp[i(\omega t + \beta_1 + \beta_2)]. \quad (4)$$

Hence, the output electric field has both vertical and horizontal components, and its amplitude is confined within the bandpass filter (BPF) nonzero values created by the  $u$  functions; see Fig. 2. (For simplicity, the frequency dependence was replaced with the wavelength.)

Since the LCR retardation is electrically controlled, the optical device may perform as a linear polarization switch by changing the retardation of the second LCR from  $\delta_2 = 2\pi m$  to  $\delta_2 = (2m+1)\pi$ —the resulting electric fields are given in Eq. (5) and Eq. (6), respectively (in terms of the wavelength):

$$\vec{E}_{OUT}|_{\delta_2=2\pi m} = u(\lambda - \lambda_{HPF})[1 - u(\lambda - \lambda_{LPF})][1 - u(\lambda - \lambda_1) + u(\lambda - \lambda_2)] \times \begin{bmatrix} \cos \delta_1/2 \\ 0 \end{bmatrix} E_{IN,0,X} \exp\left[i\left(\frac{2\pi c}{\lambda}t + \beta_1 + \beta_2\right)\right], \quad (5)$$

$$\vec{E}_{OUT}|_{\delta_2=(2m+1)\pi} = u(\lambda - \lambda_{HPF})[1 - u(\lambda - \lambda_{LPF})][1 - u(\lambda - \lambda_1) + u(\lambda - \lambda_2)] \times \begin{bmatrix} 0 \\ -i \cos \delta_1/2 \end{bmatrix} E_{IN,0,X} \exp\left[i\left(\frac{2\pi c}{\lambda}t + \beta_1 + \beta_2\right)\right], \quad (6)$$

where  $\lambda$  is the wavelength,  $c$  is the speed of light, and  $t$  is the time. The electric field in Eq. (5) is parallel to the  $x$  axis, whereas the electric field of Eq. (6) is perpendicular to the  $x$  axis. Moreover, if the first LCR is designed in accordance with the bandpass filter transmission, it is possible to choose either of the allowed bands from the BPF by controlling the retardation of the first LCR. By changing the supplied voltage for the first LCR, one may set  $\cos \delta_1/2$  to be zero for the first peak of the BPF, and  $\cos \delta_1/2$  to be a maximum for the wavelength at the second peak of the BPF. Then, by controlling the retardation of the second LCR, linear polarization switching may be performed. Alternatively, the first peak of the BPF is transmitted, and the second peak is blocked, and yet again linear polarization switching may be performed. The preceding statements are clarified by writing the intensity expression for the parallel and perpendicular polarization states,  $I_{par}$  and  $I_{per}$ , respectively:

$$I_{par} = I_{per} \propto \|\vec{E}_{OUT}\|^2 = \overbrace{u(\lambda - \lambda_{HPF})^2 [1 - u(\lambda - \lambda_{LPF})]^2 [1 - u(\lambda - \lambda_1) + u(\lambda - \lambda_2)]^2}^{U(\lambda)} \times \cos^2 \delta_1/2 \cdot E_{IN,0,X}^2, \quad (7)$$

$$= U(\lambda) E_{IN,0,X}^2 \cdot \cos^2 \delta_1/2.$$

## 2.2 Practical Characterization of the Device

The experimental setup is depicted in Fig. 3. A fiber wide spectral source (Dolan-Jenner DC-950H DC-regulated fiber optic illuminator with 150-W halogen lamp) was used to illuminate the device. (The NIR constant filter of the illuminator was extracted from the apparatus.) The emerging light was collimated by an achromatic objective lens (O). A first NIR polarizer (TECHSPEC NIR linear polarizer, extinction ratio 40 dB, 750 to 850 nm) was positioned vertically (P1), followed by a first LCR at 45-deg orientation (LCR1) and a second vertically aligned NIR linear polarizer (P2). A second LCR at 45-deg orientation (LCR2) is positioned after the second linear polarizer, followed by a long-pass (L) filter ( $\lambda > 700$  nm, Edmunds Optics,  $T > 97\%$ ), a short-pass (S) filter ( $\lambda < 950$  nm, Edmunds Optics,  $T > 60\%$ ), and a dielectric (Di) mirror (CVI Optical Components and Assemblies, TMI 800,  $R > 99\%$ ). The LC (Merck E44) retarders were constructed in our lab (clean room, grade 100). The first LCR was constructed with silica spacers with a diameter of 10 microns,

whereas the second LCR spacers were 4.7 microns in diameter. The entire stack was followed by an additional linear polarizer (A; polarization plate beamsplitter, Edmunds Optics), an achromatic collecting lens (C), a collecting optical fiber supplied with a fiber connector (FC), and a parallel spectrometer (StellarNet, Inc.). The LCRs were supplied with a 1-kHz sinusoidal wave with suitable voltages.

The absolute transmission of the device and the polarization linearity were tested. In Fig. 4, the optical normalized transmission, as well as the extinction ratio, of the device are depicted for both vertical and horizontal polarization. In Figs. 4(a) and 4(b), the transmission of the 729-nm and 922-nm vertical and horizontal polarization modes of the device are depicted, respectively. These spectral bands were chosen since their spectral regions hold both high penetration depth<sup>12,13</sup> and strong melanoma absorption.<sup>5</sup> The obtained signals are strong enough for our imaging system and have a relatively narrow band (FWHM < 25 nm). In Figs. 4(c) and 4(d), the extinction ratio was measured for both the vertical and the horizontal

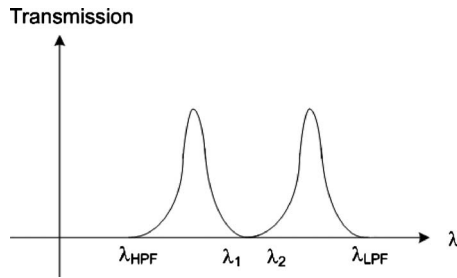


Fig. 2 Qualitative output of the bandpass filter created by the combination of an HPF, an LPF, and a suitable dielectric mirror.

polarizations of the 729-nm, and the 922-nm lines, respectively. The extinction ratio for the 729-nm line is 35 for the vertical polarization and 250 for the horizontal polarization. The extinction ratio for the 922-nm line is 10 for the vertical polarization and 72 for the horizontal polarization. Note that there is a small non-ideality both in the polarization linearity and in the filtering efficiency. However, these two factors may be further improved by an optimization process of the LCR design and construction.

### 3 Spectropolarimetric Imaging System

The spectropolarimetric imaging system is depicted in Fig. 5. A fiber bundle consisting of 50-micron core diameter optical fibers coupled to a 150-W halogen lamp source (spectral range 400 nm to 2000 nm) is used as the light guide in the optical system (dual branch light guide, Edmunds Optics). The optical-fiber connector (FC) is concentric with the objective entrance pupil. The light emerging from the objective is collimated and then linearly polarized by the first NIR linear polarizer (P1). After the first linear polarizer, a first liquid crystal retarder (LCR1) is positioned, followed by a second NIR linear polarizer (P2). LCR1 is used to pick one of the two spectral lines 729 nm or 922 nm, whereas LCR2, which is positioned right after the second linear polarizer, is used to control the direction of the transmitted linear polarization (vertical or horizontal). A metal scanning-plain-mount (SPM) is positioned at the object plane. The SPM has a circular window where the diagnosed skin is to be positioned and irradiated with approximately 50 mW/cm<sup>2</sup>. The backscattering of the object is then reflected toward an additional linear polarizer (A), which is vertically aligned, and then collected by an achromatic lens (C). A long-pass filter (L), a short-pass filter (S), and a dielectric mirror (Di) are positioned between the collection lens and the NIR CCD camera (Sony XC-E Series Monochrome CCD camera, spectral range 400 to 870 nm).

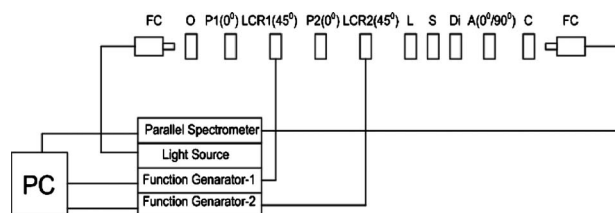


Fig. 3 The optical setup used for the characterization of the LC dual-wavelength polarization controller.

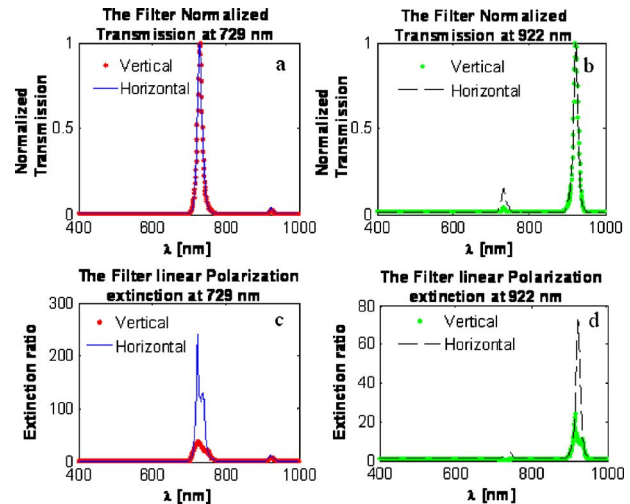


Fig. 4 The spectropolarimetric performances of the device for the 729-nm and 922-nm lines. (a) and (b): Vertical and horizontal normalized transmission of the 729-nm and 922-nm lines, respectively. (c) and (d): Vertical and horizontal extinction of the 729-nm and 922-nm lines.

The setup can photograph lesions of 15 mm × 12 mm in size, and the angle between the illuminating optical path and the imaging optical path is 40 deg, although any angle between 10 and 50 deg was checked to give similar results.

The SP imaging system is automatically controlled by MATLAB. Four different images, in less than half a second, are taken for each lesion, two for each spectral line in both horizontal and perpendicular polarizations. After acquiring the images, a simple image processing algorithm is used to enhance the quality of the image and to obtain the superficial and deep skin layer images. The method of isolating the back-scattering photons reflected by superficial skin tissue from the deeply diffused (into the dermis) dominant photons is done by subtracting the horizontal polarization image (which is the image where the impinging polarization is at crossed state with respect to the analyzer polarization orientation) from the vertical polarization image. The method assumes that linearly polarized light impinging on skin tissue is depolarized by the

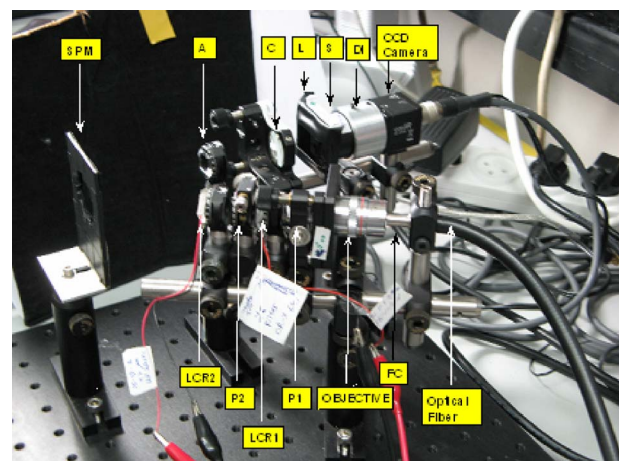
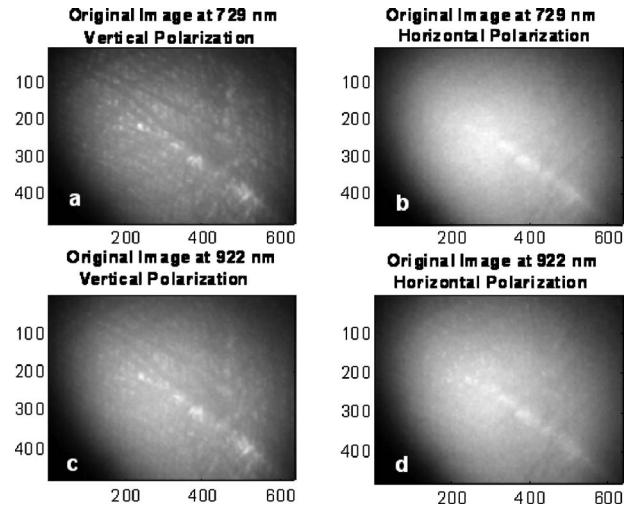


Fig. 5 The spectropolarimetric imaging system on an optical bench.

superficial skin tissue, and the deeper the light penetrates, the greater is the depolarization effect. Hence, photons reflecting backward from deep skin layers are totally depolarized, whereas photons reflecting from the more superficial skin layers maintain some certain degree of polarization. By subtracting the horizontal polarization image from the vertical one, we recover the photons that are backscattered from the superficial layer only. The method improves the quality of the surface image and hence allows a better diagnosis of the nevi nature (symmetry and borders). The preceding process is done for each wavelength, and since the scattering and penetration nature of the photons at different wavelengths are different, the process produces different depth images with excellent border appearance. In addition, by subtracting longer wavelength images from shorter wavelength images (i.e., 729-nm images subtracted from 922-nm images), deep-tissue images are revealed, allowing assessment of the lesion's deeper structure. To avoid the differences between the illumination intensity of the spectrally resolved images, before subtraction of the wavelength images, a normalization process is applied to each image, i.e., the vertical and horizontal polarimetric images of 922 nm are normalized, then the vertical and horizontal polarimetric images of 729 nm are normalized, and last, the subtractions of the two spectrally resolved images of the horizontal polarimetric images and the vertical polarimetric images are applied. To reduce the small spatial noise, the result of small movements of the subject while photographing (in spite the speed of 0.1 s at which the images are taken), we convolved all the images with a spatial Gaussian filter and thereby reduced the influence of any random noise as well as small pixel size movements of the subject. We found that a satisfying clear image is obtained by applying a Gaussian filter having a mean and variance values of 0 and 2, respectively, with a convolving matrix including  $11 \times 11$  pixels.

#### 4 Skin Imaging Results with an Optical Bench Setup

The preceding imaging method was applied to a few different lesions using the optical bench setup shown in Fig. 5 before building a suitable prototype for clinical tests. In Fig. 6, a small scar positioned on the palm of the hand was photographed. The image of Fig. 6(a) is much sharper than the image of Fig. 6(b). The photons of the image of Fig. 6(b) experienced much more scattering events, carrying tissue information from a deeper skin layer; hence, they are more depolarized by the many scattering events. Note that the deformed scar tissue is seen under the superficial epidermal layer. In Fig. 6(a), the superficial layer of the skin is visualized. The photons of the image of Fig. 6(a) are photons that maintain their polarization since they are backscattered from the superficial layer of the skin. Figures 6(c) and 6(d) are similar images to those in Figs. 6(a) and 6(b) except for the different wavelength. Note that there are resolution differences between the wavelength images of 729 nm and 922 nm, which occurs because the penetration depth of the 922-nm photons is greater than that for the 729-nm photons so that different tissue depth images are obtained; therefore the images at 922 nm are more blurred. In Fig. 7, the scar images after the simple image processing are depicted. In Fig. 7(a), the difference image of the image at 922 nm and that at



**Fig. 6** Vertical and horizontal images of a scar located on the palm of a white Caucasian: (a) vertical image at 729 nm, (b) horizontal image at 729 nm, (c) vertical image at 922 nm, and (d) horizontal image at 922 nm. The images have a horizontal-by-vertical size of 15 mm  $\times$  10 mm.

729 nm with vertical polarization is presented. Note that it highlights the bottom of the scar. The image in Fig. 7(b) is too blurred, apparently because the horizontal images at both 729 nm and 922 nm are too blurred. However, the polarimetric images at 729 nm and 922 nm are with high resolution, and many details are exposed. Note that in each of the images [apart from the image in Fig. 7(b)], the borders and the shape of the scar are highly defined.

In Fig. 8, images of a 3-mm seborrheic keratosis on the dorsal side of the palm of a white Caucasian subject is treated by cryosurgery. Note [Figs. 8(a) and 8(c)] that the contour of the lesion is well defined. Figure 8 and Fig. 6 represent two different subjects under identical technical imaging conditions. Figure 9 is the same image as in Fig. 8 after applying the simple image processing algorithm. Note that in Fig. 9(a),

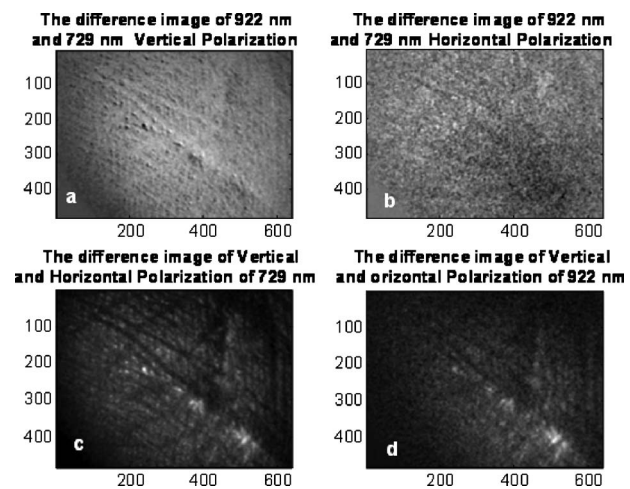


**Fig. 7** Polarimetric and spectral image processing: (a) spectral vertical difference image, (b) spectral horizontal difference image, (c) polarimetric image at 729 nm, and (d) polarimetric image at 922 nm. Each image has a horizontal-by-vertical size of 15 mm  $\times$  10 mm.

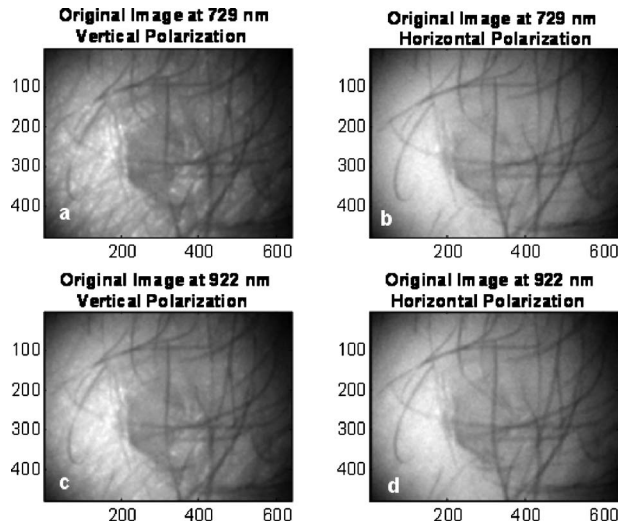


**Fig. 8** Vertical and horizontal images of a seborrheic keratosis treated by cryosurgery (tissue destruction by freezing): (a) vertical image at 729 nm, (b) horizontal image at 729 nm, (c) vertical image at 922 nm, and (d) horizontal image at 922 nm. The images have a horizontal-by-vertical size of 15 mm × 10 mm.

it seems that the deeper part of the lesion is represented, with the contours easily recognized. In Fig. 9(b), the contour of the lesion is also seen, and in Figs. 9(c) and 9(d), the edges of the lesion, in two different tissue depths, are furthered enhanced. We examined the lesion after the frozen tissue was removed and found that indeed the shape of the cavity was very similar to the image of Fig. 9(d). We then concluded that the image is indeed the image of the lesion bottom surface borders, and by measuring the width of the dead skin, we could estimate the penetration capabilities of the device. The thickness of the frozen tissue was over one millimeter, which we estimate to be roughly the optical penetration capability.

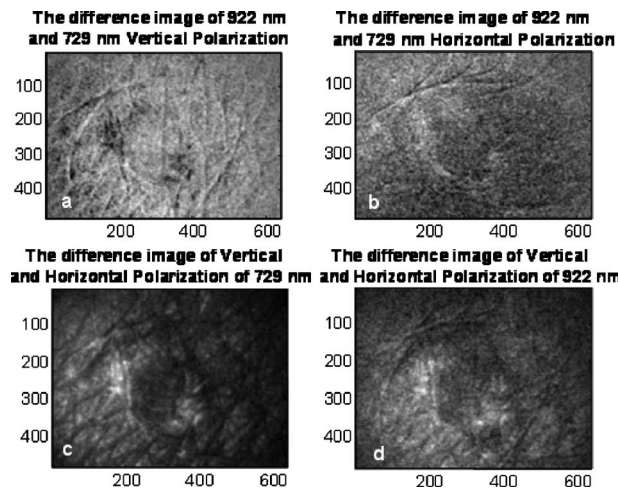


**Fig. 9** Polarimetric and spectral image processing of a seborrheic keratosis treated by cryosurgery: (a) spectral vertical difference image, (b) spectral horizontal difference image, (c) polarimetric image at 729 nm, and (d) polarimetric image at 922 nm. The images have a horizontal-by-vertical size of 15 mm × 10 mm.

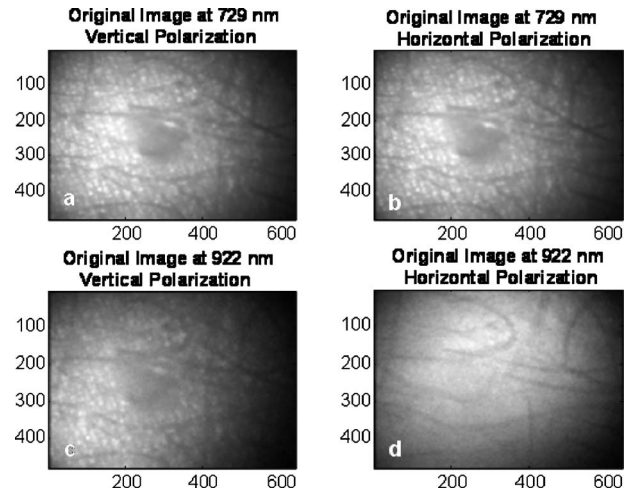


**Fig. 10** Vertical and horizontal images of a nontreated seborrheic keratosis: (a) vertical image at 729 nm, (b) horizontal image at 729 nm, (c) vertical image at 922 nm, and (d) horizontal image at 922 nm. The images have a horizontal-by-vertical size of 15 mm × 10 mm.

In Fig. 10, images are shown of nontreated seborrheic keratosis, 2.5 mm in diameter, which is located on the hand of a white Caucasian subject. The lesion protrudes about a half-millimeter above the superficial layer of the skin. Note that the lesion is not seen in Fig. 10(d), apparently because the imaged tissue is deeper than the lesion borders. Figure 11 is the image of Fig. 10 after applying the simple image processing. Note that in Fig. 11(a), it seems as if the lesion's deep border has been demonstrated and that the contour of the lesion in the deep tissue is easily recognized. In Fig. 11(b), apparently a less deep tissue level was imaged, and here as well, the contour of the lesion is easily seen. In Fig. 11(c), the boundaries of the superficial layer of the lesion are further enhanced. The image reveals the precise borders of the lesion

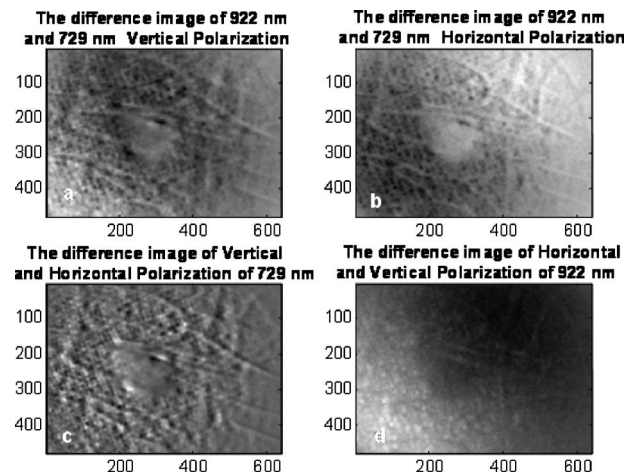


**Fig. 11** Polarimetric and spectral image processing of a nontreated seborrheic keratosis: (a) spectral vertical difference image, (b) spectral horizontal difference image, (c) polarimetric image at 729 nm, and (d) polarimetric image at 922 nm. The images have a horizontal-by-vertical size of 15 mm × 10 mm.



Fig. 12 The V-imager clinical prototype.

along with its spatial structure—it is easy to recognize the protrusion of the lesion above the surrounding skin.

## 5 Skin Imaging Results with a Clinical Prototype

The experimental setup was assembled into a useful compact clinical module. The module is presented in Fig. 12. It is constructed of two movable arms in a tilted V-shape that comprises the optical components as described in the experimental setup. The body of the prototype module was fabricated using an STL printer (stereo lithography printer of Objet). The angle between the arms is 25 deg, and the total length of the device is 30 cm. Due to its shape, we called the device simply V-imager. The V-imager comprises a circular window at the object plane with a diameter of 23 mm, allowing imaging and assessment of such size lesions. The V-imager was used in the Department of Plastic Surgery at Soroka University Hospital in Beer Sheva, Israel. An example of a characteristic image of a compound nevus of a white Caucasian subject is depicted in Fig. 13.

Figure 13 is identical to Fig. 11 in all aspects except for the imaged object. Note that the contours of the lesion as well as some pigmentation differences are easily seen. Naked eye ob-

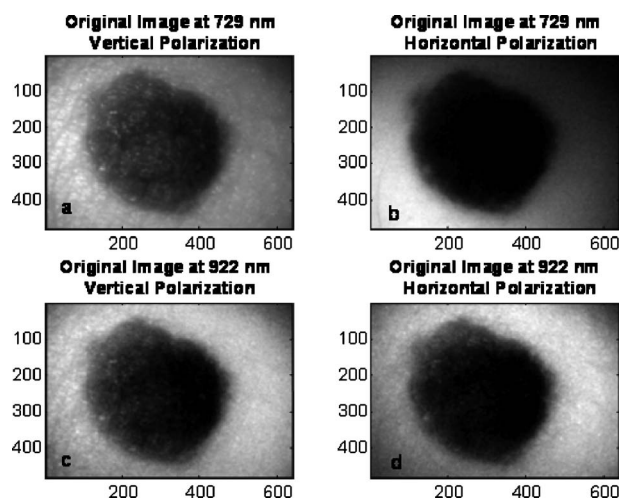


Fig. 13 Vertical and horizontal images of a compound nevus of a white Caucasian subject: (a) vertical image at 729 nm, (b) horizontal image at 729 nm, (c) vertical image at 922 nm, and (d) horizontal image at 922 nm. The images have a horizontal-by-vertical size of 15 mm×10 mm.

The difference image of 922 nm and 725 nm after polarimetric image subtraction

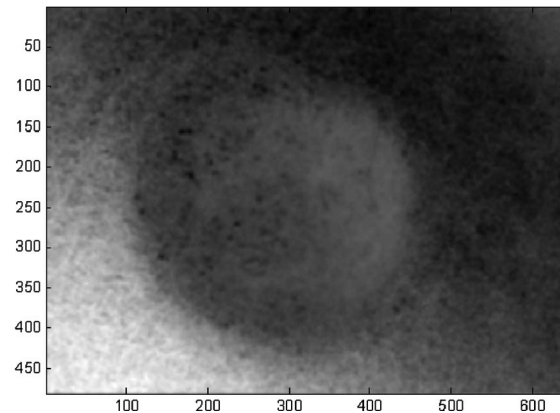


Fig. 14 Polarimetric and spectral difference image of a compound nevus of a Caucasian subject. The image has a horizontal-by-vertical size of 15 mm×10 mm.

servation of this lesion does not reveal any pigmentation differences and it is impossible to assess its distribution beneath the skin superficial layer. To obtain the image in Fig. 14, first the vertical polarization image at 729 nm is subtracted from the vertical polarization image at 922 nm to create the vertical polarization wavelength difference image. Second, the horizontal polarization image at 729 nm is subtracted from the horizontal image at 922 nm to create the horizontal polarization wavelength difference image. Then, to achieve the image in Fig. 14, the horizontal polarization wavelength difference image is subtracted from the vertical polarization wavelength difference image.

In Fig. 14, it seems as if the nevus's deep border has been demonstrated and its contour in the depth of cutaneous tissue is easily recognizable. By subtraction of the vertical polarization of the spectrally resolved images, we obtain an image of the deep skin layer that is not depolarized. By subtraction of the horizontal polarization of the spectrally resolved images, we obtain an image of the deep skin layer that is grossly depolarized. By subtracting these two images, we eliminate the backscattering from the vertical difference image, thus obtaining a sharp image of the contour of the object underneath the superficial layer.

## 6 Conclusions

A novel concept is proposed for spectropolarimetric imaging using specially designed LC devices incorporated into a miniature imaging module used for skin imaging. The LC device characteristics matched the theoretical design. It should be pointed out that by using additional dielectric mirrors (for example, dielectric mirrors with central wavelengths of 500 nm and 700 nm), along with a shorter pass filter (for example, a short-pass filter of  $\lambda > 400$  nm and a long-pass filter  $\lambda < 800$ ), more spectrally resolved images can be obtained. In this respect, a 400-nm spectrally resolved image will provide additional information, since melanoma skin cancer cells tend to strongly absorb this wavelength. The implementation of the SP system along with a simple image processing algorithm produced an SP images set that can help clinicians to differentiate the precise borders and shape of a

lesion on the surface and deeper below the epidermal tissue. The system was tried on a small scar, an untreated and a treated seborrheic keratosis, and a compound nevus of white Caucasian subjects. The result showed clear images of the shape and borders of the superficial layer of the lesions along with, what we believe to be, deep epidermal tissue. A clinical prototype was designed, built, and used to obtain more SP images of patients in the hospital and to collect more data that eventually may allow diagnosing skin cancer, and in particular melanoma skin cancer, in early stages. The system is unique in several aspects: it is fast, compact, and not costly; it has no mechanical moving parts; it uses a halogen lamp illumination, which allows a wide spectrum along with true color imaging; and it applies NIR spectra and thus has penetration capabilities deep below the epidermis.

### References

1. A. N. Yaroslavsky, V. Neel, and R. R. Anderson, "Demarcation of nonmelanoma skin cancer margins in thick excisions using multispectral polarized light imaging," *J. Invest. Dermatol.* **121**, 259–266 (2003).
2. N. Rajaram, T. J. Aramil, K. Lee, and J. W. Tunnel, "Clinical instrument for spectral diagnosis of cutaneous malignancy," *Proc. SPIE* **6848**, 68480R-1 (2008).
3. N. Rajaram, T. H. Nguyen, and J. W. Tunnel, "Lookup table-based inverse model for determining optical properties of turbid media," *J. Biomed. Opt.* **13**(5), 050501-1–050501-3 (2008).
4. P. Daukantas, "Using optics to detect skin cancer," *Opt. Photon. (OPN)* **November**, 27–33 (2007).
5. J. T. Oh, M. L. Li, H. F. Zhang, K. Maslov, G. Stoica, and L. V. Wang, "Three-dimensional imaging of skin melanoma *in vivo* by dual-wavelength photoacoustic microscopy," *J. Biomed. Opt.* **11**(3), 034032-1–034032-4 (2006).
6. N. D. Galdkova, G. A. Petrova, N. K. Nikulin, S. G. Radenska-Lopovok, L. B. Snopova, Yu. P. Chumakov, V. A. Nasonova, V. M. Gelikonov, G. V. Gelikonov, R. V. Kuranov, A. M. Sergeev, and F. I. Feldchtein, "In vivo optical coherence tomography of human skin," *Skin Res. Technol.* **6**, 6–16 (2000).
7. J. Welzel, E. Lankenau, R. Bringruber, and R. Engelhardt, "Optical coherence tomography of human skin," *J. Am. Acad. Dermatol.* **37**, 958–963 (1997).
8. T. Gambichler, A. Orlikov, R. Vasa, G. Moussa, K. Hoffmann, M. Stucker, P. Altmeyer, and F. G. Bechara, "In vivo optical coherence tomography of basal cell carcinoma," *J. Dermatol. Sci.* **45**, 167–173 (2007).
9. J. S. Baba, J. R. Chung, A. H. DeLaughter, B. D. Cameron, and G. L. Coté, "Development and calibration of an automated Mueller matrix polarization imaging system," *J. Biomed. Opt.* **7**(3), 341–349 (2002).
10. S. L. Jacques, J. C. Ramella-Roman, and K. Lee, "Imaging skin pathology with polarized light," *J. Biomed. Opt.* **7**(3), 329–340 (2002).
11. J. C. Ramella-Roman, K. Lee, S. A. Prahl, and S. L. Jacques, "Design, testing, and clinical studies of a handheld polarized light camera," *J. Biomed. Opt.* **9**(6), 1305–1310 (2004).
12. S. G. Demos and R. R. Alfano, "Optical polarization imaging," *Appl. Opt.* **36**(1), 150–155 (1997).
13. S. G. Demos, H. B. Radousky, and R. R. Alfano, "Deep subsurface imaging in tissues using spectral and polarization filtering," *Opt. Express* **7**(1), 23–28 (2000).
14. O. Aharon and I. Abdulhalim, "Liquid crystal Lyot tunable filter with extended free spectral range," *Opt. Express* **17**, 11426–11433 (2009).
15. O. Aharon and I. Abdulhalim, "Tunable optical filter having a large dynamic range," *Opt. Express* **34**, 2114–2116 (2009).
16. A. Safrani and I. Abdulhalim, "Liquid-crystal polarization rotator and a tunable polarizer," *Opt. Express* **34**, 1801–1803 (2009).
17. R. C. Jones, "A new calculus for the treatment of optical systems," *J. Opt. Soc. Am.* **31**, 488–493 (1941).